Tailoring the oxide surface composition of stainless steel for improved OER performance in alkaline water electrolysis

Hamid Reza Zamanizadeh [a], Svein Sunde [a], Bruno G. Pollet [b,c], Frode Seland [a,*]

[a] Department of Materials Science and Engineering, Norwegian University of Science and Technology (NTNU), NO-7491 Trondheim, Norway
[b] Hydrogen Energy and Sonochemistry Research Group, Department of Energy and Process Engineering, Norwegian University of Science and Technology (NTNU), NO-7491 Trondheim, Norway
[c] Pollet Research Group, Hydrogen Research Institute (HRI), Université du Québec à Trois-Rivières, 3351 Boulevard des Forges, Trois-Rivières, Québec G9A 5H7, Canada

A R T I C L E   I N F O

A B S T R A C T

There is a strong desire to replace bulk nickel electrodes for oxygen evolution reaction (OER) with a cheaper and more active steel material in alkaline water electrolyser (AWE). However, implementing an activation procedure to optimize the steel electrode surface is necessary. In this work, we activated 316 stainless steel (SS316) in KOH electrolytes of increasing concentration by applying an optimized potential of +1.70 V vs RHE for 18 hours. The electrocatalytic activity increased significantly with increasing the KOH concentration of the activation electrolyte, which is linked to a beneficial change in the surface composition during activation. The surface was analysed using X-ray Photoelectron Spectroscopy (XPS), Glow Discharge - Optical Emission Spectroscopy (GD-OES) and Scanning Electron Microscopy (SEM). XPS showed an increasing Ni content (41% to 73%) in the surface with simultaneous removal of Cr (3.4% to 0%) and Fe (55% to 27%) with increasing KOH concentration of the activation electrolyte. Activation in minimum 7.5 M KOH gave the best performing OER electrode with an electrode potential (E) of +1.525 V vs. RHE at a current density (j) of 10 mA cm^{-2}. Tafel slopes of around 40 mV dec^{-1} were found for all activated samples, indicating the same OER mechanism independent of the resulting surface composition. Reaction orders of 1.5 and 1.3 were found in the low and high potential regions, respectively. A negligible performance change was observed for the activated electrodes over a 48 h test at 10 mA cm^{-2} in 1.0 M KOH. This work shows that the electrochemical activation of 316 stainless steel in high pH KOH electrolytes improves the OER activity significantly and that the surface composition can be tailored with KOH concentration up to 73% Ni. Through optimizing the surface composition, steel materials offer a cost-effective alternative to bulk nickel electrodes as OER electrodes in commercial AWE.

1. Introduction

Splitting water into molecular oxygen (O$_2$) and hydrogen (H$_2$) is thermodynamically unfavorable, and it therefore requires energy input for the reactions to proceed. In water electrolysis, a substantial overvoltage is required to overcome the irreversible losses in the cell related to primarily electrode kinetics, ohmic resistance and mass transport. The oxygen evolution reaction (OER) at the anode is known to contribute with a relatively large portion of this overvoltage and a lot of work has been dedicated to understanding this reaction mechanism and in designing an optimum electrocatalyst [1–3]. A suitable OER electrode must offer (i) large surface area, (ii) fast reaction kinetics, (iii) high electrical conductivity, (iv) high durability, (v) availability and low cost,

(vi) scalability, (vii) recyclability and (viii) minimum HSE risks in its production, use and recycling.

Platinum group metal (PGM) oxides, such as RuO$_2$, and IrO$_2$ possess excellent catalytic activity towards the OER in both acidic and alkaline electrolytes, but widespread application as catalysts are restricted due to their low abundance and high cost [4]. Cost-efficient and electrochemical active transition metal mixed oxides (TMMO) are promising OER catalysts in alkaline media and thus have been extensively studied [4–8]. Among them, massive attention has been dedicated to Ni-based OER catalysts since they are earth-abundant and have theoretically high catalytic activity [3,4,9,10]. Several studies on the various Ni-bimetallic catalysts confirm that adding Fe results in the lowest overpotential for OER [11–16]. Even small amount of Fe precipitated

---

from the electrolyte on the Ni surface was found to have a huge impact on the OER activity [17–19]. This finding has led to the syntheses of various NiFe compounds in order to understand the role of Fe and optimize OER Ni-Fe electrocatalysts [20–24].

Landon *et al.* [25] prepared mixed Fe-Ni oxides using evaporation induced self-assembly, hard templating, and dip-coating, and realized that there is a peak in intrinsic OER activity with around 10 mol% Fe content, independent of the preparation method. They associated the increased activity with formation of a $NiFe_2O_4$ phase at low Fe concentrations. In addition, a segregated Fe_2O_3 phase was found at compositions above 25 mol% possessing a lower OER activity. This is in line with Friebel *et al.* [26], who reported a high catalytic OER activity of NiFe with around 10-25% Fe and demonstrated that the catalytic phase is γ-$Ni_{1-x}Fe_xOOH$ formed at Fe levels below 25%. Again, a separate γ-FeOOH phase was found to nucleate for Fe levels above 25% leading to a lower OER activity. Interestingly, their DFT calculations showed that Fe^{3+} in γ-$Ni_{1-x}Fe_xOOH$ in fact exhibited a significantly lower overpotential than Ni^{3+} in either γ-$Ni_{1-x}Fe_xOOH$ or γ-NiOOH [26]. Burke *et al.* [16] also suggested that Fe represents the essential active material and substitutes Ni to form an active $Ni(Fe)O_xH_y$ surface, with Ni maintaining a high electrical conductivity and offering a large surface area. The hypothesis that Fe acts as active site is supported by the experimental work of Ahn *et al.* [27], where two types of surface sites with "fast" and "slow" kinetics were found by SECM on a $Ni_{1-x}Fe_xOOH$ film and the fraction of "fast" sites matched the Fe content in the film. Despite the apparent promoting effect of Fe additions, various optimum Ni to Fe ratios for OER activity are reported. Singh *et al.* [28] studied OER on electrodeposited Ni-Fe alloys on mild steel in 1 M KOH at 25C and found that 17.9% Fe gave the best performing electrode (highest exchange current density and in addition the lowest Tafel slope, around 40 mV dec^{-1}). Louie and Bell [21] reported maximum OER activity with 40% Fe in a Ni-Fe film. Gorlin *et al.* [29] investigated the amorphous Ni-Fe behaviour in 0.1 M KOH and noticed an abrupt increase in the OER activity with introducing over 9% Fe in to the $Ni_{100-x}Fe_x$. They suggested to have a Ni-Fe(OOH) bimetallic phase instead of separate Fe and Ni-oxide phases, with around 50% Fe as the optimum composition for OER. Qiu *et al.* [30] analyzed the OER activity of $Ni_yFe_{1-y}O_x$ amorphous nanoparticles supported on carbon in 1.0 M KOH and showed that $Ni_{0.69}Fe_{0.31}O_x$/C exhibited a 280 mV overpotential at 10 mA cm^{-2} outperforming those with 17, 54 and 75% Fe. Corrigan [18] depicted that 10-50% Fe co-precipitated into a thin nickel oxide film has the most effect in lowering the OER overpotential. In general, there is undoubtedly a beneficial effect of adding Fe to Ni towards the OER activity, but no consensus about the optimum Ni to Fe ratio is reached other than that a minimum 50% surface Ni seems to be required.

More recently, stainless steel electrodes with low amount of Ni have gained increased attention as OER electrodes in alkaline media [31–40]. According to Maurice *et al.* [41], there is no Ni in the surface layer on untreated stainless steel (Fe-18Cr-13Ni). Hence, a surface enrichment of Ni is needed to obtain a satisfactory OER activity. Also, identifying the effect on catalytic properties of other components present in the steel materials is important in developing an optimized surface treatment. For example, Cr was found to be effective to increase the OER activity of $NiFe_{2-x}Cr_xO_4$ ($0 \leq x \leq 1$) [42], and thus the surface ratio of Ni-Fe-Cr must be modified for improved OER activity in Cr-containing stainless steels such as SS316 and SS304. Several pretreatments are reported leading to more active surfaces. Schäfer *et al.* [32] modified the surface of AISI304 steel at 293 K by exposing it to chlorine (Cl_2) gas and obtained a more active surface oxide layer enriched with Fe and Cr. Anantharaj *et al.* [35] oxidized SS304 in an equimolar solution of KOH and hypochlorite at 180°C for 12 hours and found a Fe-Cr-Ni metal-oxide enriched surface improving the OER activity. Similar surface modification and OER improvement were achieved by Zhong *et al.* [36] using a hydrothermal treatment of stainless steel in ammonium solution at 200°C followed by electrochemical cycling in 1.0 M KOH from -1.4 to +0.5 V vs. SCE with a scan rate of 50 mV s^{-1}. Moureaux *et al.* [31,43] Schäfer *et al.* [33]

Table 1

Overview of the activated samples produced with names in accordance with the KOH concentration used during the electrochemical activation

Sample name	Substrate	KOH concentration
SS1	SS316	1.0 M KOH
SS3	SS316	3.0 M KOH
SS5.5	SS316	5.5 M KOH
SS7.5	SS316	7.5 M KOH
SS10	SS316	10 M KOH
SS12.5	SS316	12.5 M KOH

electro-oxidized different types of steel in alkaline media and obtained Ni-enriched surfaces again improving OER activity.

Among the used methods, electro-oxidation of stainless steel in alkaline media represents both a simple and promising method to enrich the surface with Ni, significantly improving OER activity [31,33,43]. Furthermore, different surface compositions can be obtained from electrooxidation of stainless steels depending on substrate material, potential and electrolyte [44–46]. It is imperative to study the pretreatment conditions in greater detail to identify the conditions leading to a Ni-Fe-Cr surface composition that optimizes the OER activity.

In this work, we change the surface composition of stainless steel 316 through electro-oxidation in KOH electrolytes of different concentrations, and study the resulting composition and activity towards the OER. The resulting Ni-Fe-Cr surface was studied using SEM, Raman Spectroscopy, GD-OES and XPS, and is shown to depend on time, electrode potential and KOH concentration used in the activation electrolyte. Linear sweep voltammetry (LSV) and cyclic voltammetry (CV) of the prepared electrodes were performed in 1.0 M KOH and used to identify the optimum activation procedure and surface composition towards the OER. Reaction order and electrochemical surface area were also determined from LSV and CV experiments, respectively.

2. Experimental

2.1. Sample preparation and electrochemical activation

A three-electrode electrochemical cell of conventional design made from Teflon (PTFE) was used in the electrochemical activation and subsequent electrochemical characterization. The working electrode (WE) consisted of a stainless steel 316L (SS316: 10-14% Ni, 16-18% Cr, min. 69% Fe, etc.) plate material that was cut into disc-shaped samples ($\varnothing$ 5 mm), fixed with a conductive wire and molded in epoxy. The front side of the molded electrode was polished with 800, 1200 and 2200 SiC abrasive papers to a mirror finish and then ultrasonically (bath, 40 kHz, 185 W, duration = 15 mins) cleaned in a water bath before electrochemical activation. All samples, including untreated and etched samples, were initially polished in accordance to the procedure above. The etched sample was subsequently etched in a freshly prepared mild aqua regia electrolyte for 10 minutes (4.75 ml concentrated HCl mixed with 1.1 ml concentrated HNO_3 and diluted to 50 mL total volume with milliQ water).

A Hg/HgO, KOH (20%) (Koslow Scientific Company) and a silver (Ag) wire wrapped around a PEEK rod were used as reference electrode (RE) and counter electrode (CE), respectively. All measurements were performed at room temperature (22 ± 1°C) and potentials are converted and presented with respect to a reversible hydrogen electrode (RHE), unless otherwise stated. The potential between the WE and the RE or the current through the CE circuit was controlled using a Gamry Reference 600™ potentiostat/galvanostat.

Prior to electrochemical activation, cyclic voltammetry experiments on the polished, *as-received* stainless steel electrodes were performed between -0.22 V to +1.50 V vs. RHE in 1.0 M KOH at a scan rate of 100 mV s^{-1} in order to identify the oxidation and reduction peaks and to assess the quality of the sample.

The polished SS316 electrodes were subsequently activated at a

constant potential of +1.70 V vs. RHE in 1.0 M, 3.0 M, 5.5 M, 7.5 M, 10 M and 12.5 M KOH solutions for 18 hours. Lower activation potentials of +1.50 and +1.60 V were also used, but only in 7.5 M KOH electrolytes. Table 1 summarizes the various samples prepared at +1.70 V for 18 hours with the associated sample names. The electrolytes were made up of KOH pellets (Merck, > 85%, product number 105033 for analysis EMSURE®) dissolved in Milli-Q water (18.2 MΩ). The electrolytes were purged with N_2 (5.0, Linde) for 30 min before and during each experiment.

2.2. Electrochemical characterization

Slow linear sweep voltammetry (LSV) experiments were performed in 1.0 M KOH electrolyte between +1.48 V to +1.68 V vs. RHE at a scan rate of 5 mV min^{-1} (0.0843 mV s^{-1}). These measurements were repeated at least three times and the average of the measurements are reported. A subsequent negative-going scan from +1.68 V down to +1.48 V was performed in all cases with a negligible hysteresis. Only the positive-going scans were used, except for SS10 and SS12.5, where the average scans were used due to a small hysteresis.

Electrochemical surface area (ECSA) of the samples were estimated based upon measured capacitance and assuming that the specific capacitance does not change with composition. The capacitance values were extracted from CV measurements between +0.65 V to +0.75 V vs RHE for scan rates of 20, 50, 100, 200 and 500 mV s^{-1}, and obtained as the slope of the plot of current (at +0.70 V) vs. scan rate [47]. It was assumed that no faradaic reactions occur in this potential region.

Electrochemical impedance spectroscopy (EIS) experiments were carried out at open circuit potential (OCP) with a voltage perturbation of 10 mV from 100 kHz to 0.01 Hz. The electrolyte resistance value (*R*) was estimated from the impedance spectrum as the high frequency intercept of the real axis in a complex impedance plot. All measured potentials in the slow linear sweep polarizations are *IR* corrected using the following equation:

$$E_{IRcorrected} = E - IR \qquad (1)$$

Where *I* is the measured current and *R* is 85% of the measured resistance of the electrolyte from EIS.

Reaction order measurements on SS7.5 were performed using five different KOH electrolytes with different pH values. The pH of the electrolyte was controlled using a pHep©5 pH/temperature tester (Hanna Instruments, 0.01 pH resolution), and was measured to be 14.35 (1.0 M KOH), 14.15 (0.50 M KOH), 13.95 (0.30 M KOH), 13.54 (0.10 M KOH) and 12.98 (0.10 M KOH + 0.90 M NaClO$_4$). The ionic strength of the solutions with pH lower than 14.35 were maintained constant by addition of K$_2$SO$_4$ for the reaction order measurement, except for the last one, where NaClO$_4$ was used. The observed reaction orders were measured at constant ionic strength, while keeping the liquid junction potentials as low as possible by employing the same electrolyte in the working electrode and reference electrode compartments.

2.3. Physical characterization

Surface morphology was studied using high resolution FESEM (Zeiss Ultra 55) with a working voltage of 10 kV. The images were captured using a secondary electron detector. The structural fingerprint of the surface was analyzed by Raman spectroscopy. All Raman spectra were obtained using a confocal Raman microscope (Witec Alpha 300R) in a backscattering geometry with a spectral resolution of 1 cm^{-1}. The spectra were collected over a range of wavenumbers, from 100 cm^{-1} to 3,800 cm^{-1}, with an excitation wavelength of 532 nm (Nd:YAG laser operating at 40 mW power). Illumination and detection were performed through a microscope objective of 50X magnification with numerical aperture of 0.75.

Elemental depth profiles of the samples were acquired using a Pulsed RF Glow Discharge Optical Emission Spectrometer (Horiba GD-Profiler
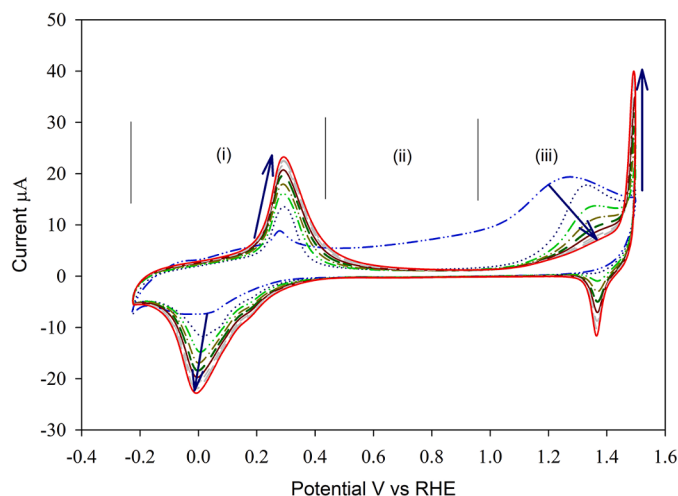

Fig. 1. A series of nine (9) consecutive cyclic voltammograms recorded on polished as-received SS316 in 1.0 M KOH at a scan rate of 100 mV s^{-1} in the potential window -0.22 to 1.5 V vs. RHE. The first scan commenced at -0.22 V vs. RHE, while the last scan ended at +1.5 V vs. RHE.

2^{TM}). A high-alloyed steel (JK 49) was used to calibrate the instrument before each measurement. Each analysis was recorded until a plateau was reached, representing the bulk composition.

The elemental composition and oxidation state of the surface were collected using an Axis Ultra DLD XPS instrument (Kratos Analytical, Manchester, UK) with a monochromatic Al X-ray source. The X-ray source was emitted at the current of 10 mA with an accelerating voltage of 10 kV. The binding energies were calibrated based on the C 1*s* peak position (284.4 eV) corresponding to adventitious carbon. Shirley background was subtracted from all XP spectra to deconvolute and evaluate the cationic composition. Relative quantities of Ni, Fe and Cr were estimated using the CasaXPS software. Ni 2*p*, Cr 2*p* and Fe 3*p* peaks were used to obtain the sample composition. Fe 2p has overlap with the Ni Auger peaks when using Al source.

All physical surface characterizations were done ex-situ after exposing the sample for ambient conditions. The stability of the surface composition of the activated steel electrode in ambient conditions was verified at two different times using XPS, with negligible changes in the surface with time. Nevertheless, all XPS, GD-OES and SEM measurements were done within one day after in-situ activation.

3. Results and discussion

3.1. Electrochemical characterization and OER activity

Cyclic voltammetry experiments on polished *as*-received SS316 sample were performed in 1.0 M KOH at room temperature to assess the redox behaviour and stability of the surface between the onsets of hydrogen (HER) and oxygen evolution reactions (Fig. 1). The first cycle was distinctly different than the subsequent cycles and the resulting voltammogram can be divided into three distinct potential regions, as indicated in Fig. 1. (i) -0.22 to +0.50 V associated with the Fe redox processes [48], (ii) +0.50 to about +1.1 V indicating a passive region and, (iii) +1.1 V to upper reversal potential (+1.50 V) where the redox reactions of Cr^{3+}/Cr^{6+} and Ni^{2+}/Ni^{3+} are expected to occur [48]. The main reason why the first and subsequent cycles were so different is due to the oxidation and partial removal of a protective surface oxide during the high positive potentials applied, i.e., linked to the fairly high oxidation current observed in the first cycle through region (ii) and (iii), and subsequent reduction of the oxide in the negative-going scan. Reduction, oxidation, and dissolution of surface species during voltammetry roughen and expose more of the underlying substrate in
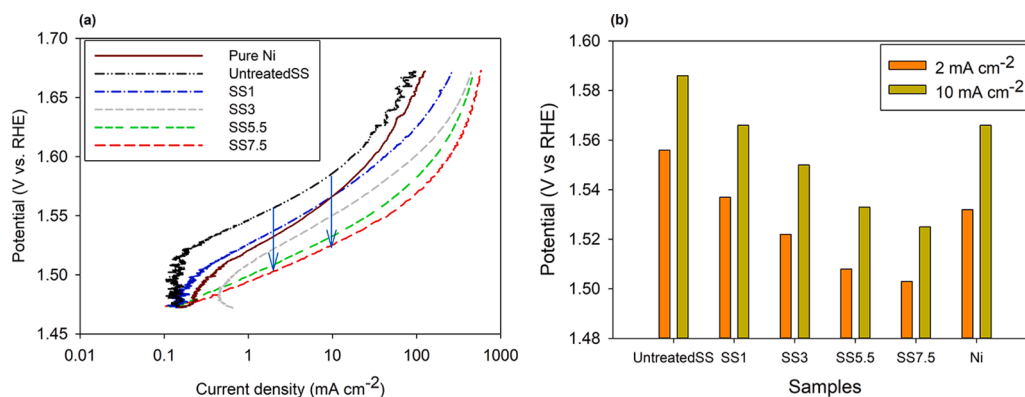
Fig. 2. (a) E vs. log(j) of SS1, SS3, SS5.5 and SS7.5 samples in 1.0 M KOH at a scan rate of 5 mV min^{-1}. (b) Corresponding OER overpotentials and onset potentials extracted from (a) at 10 mA cm^{-2} and 2 mA cm^{-2}, respectively. Non-activated SS316 and pure Ni samples are provided for comparison. The data are normalized based upon the geometric surface area.

subsequent scans until a stable surface is reached. Therefore, the charge passed during the oxidation wave in region (i) during the first cycle is low (19.4 μC) and increased significantly in subsequent cycles due to exposure of freshly reduced iron in the negative-going sweep (42.5 μC in the 9th cycle), eventually reaching a more or less stable voltammogram. This implies that the amount of Fe in the surface reaches a constant value. Similarly, a marked increase in current is observed near the upper reversal potential (+1.5 V) for all cycles except for the first one, which is either due to the Ni^{2+}/Ni^{3+} oxidation or the OER or both. The formation of a subsequent reduction wave at +1.4 V in the negative-going scan supports the former. Previous works have shown that formation of β-NiOOH and subsequent reduction occurs in this potential region, see e. g. Alsabet *et al.* [49].

A high nickel content in the surface is necessary to obtain high OER activity. According to the voltammogram and stability regions for Fe, Ni and Cr suggested in Pourbaix (*E-pH*) diagrams of Fe-Ni-Cr alloy, it seems necessary to treat the electrode at high electrode potentials and high pH values, > +1.5 V and > pH 14. Pourbaix diagrams were extracted using the *Outotec HSC Chemistry Software* and are provided in the

supplementary information (See Figure S1).

An activation potential of +1.70 V was found to be much more effective than activation potentials of +1.60 and +1.50 V in 7.5 M KOH electrolytes (see Figure S2). Moreover, an optimized activation duration of 18 hours was chosen as we found negligible changes in the catalytic activity for longer activation times (up to 54 hours, see Figure S3). The activation potentials lie in the potential region where Cr and segregated Fe are expected to dissolve. However, Ni and Fe incorporated into Ni form stable oxides [50], and the resulting surface can be expected to be rougher and contain more Ni. Furthermore, dissolution of surface components can also occur in combination with deposition of metal oxides from dissolved ions in solution, as suggested previously by Moureaux *et al.* [31].

Concentration of the activation electrolyte is found to affect the OER activity of the electrode. Linear sweep voltammetry (LSV) experiments of the activated SS316 samples at +1.70 V in various KOH concentrations, non-activated, polished SS316 and pure Ni samples are displayed as *E*-log*j* in Fig. 2(a) along with the extracted electrode potentials at 10 mA cm^{-2} and 2 mA cm^{-2} in Fig. 2(b). The activation procedure has a
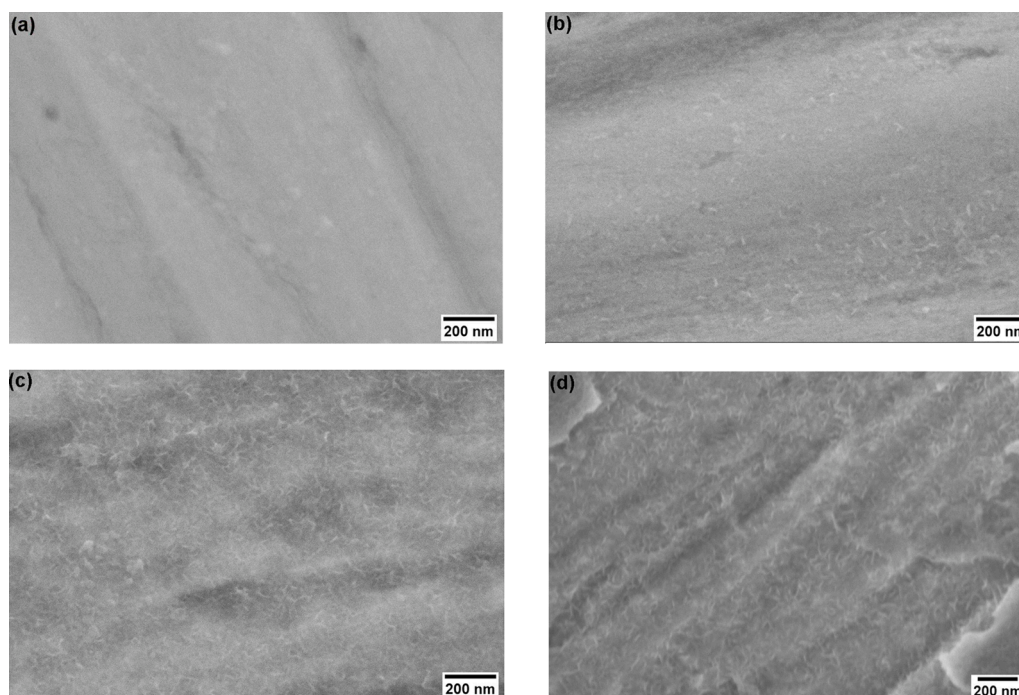

Fig. 3. SEM images of (a) untreated, (b) SS1, (c) SS5.5 and (d) SS7.5 samples.

Table 2
Metallic composition of the samples obtained by XPS

Sample	Fe (±4%)	Ni (±4%)	Cr (±0.5%)
Untreated SS316	87	0	13
Etched SS316	56.4	0	43.6
SS1	55.1	41.5	3.4
SS3	47.1	49.6	3.3
SS5.5	32.9	65.9	1.2
SS7.5	27.3	72.7	0
SS10	27.7	72.3	0
SS12.5	Not investigated		

significant impact on the OER performance, increasing with KOH concentration of the electrolyte during activation up to 7.5 M KOH. Increasing the KOH concentration to 10.0 M and 12.5 M did not affect the activity (see Figure S4). 10 mA cm^{-2} was reached at $E = +1.525$ V for the SS7.5 sample, about 60 mV lower than the non-activated polished SS316 sample ($E = +1.585$). The corresponding overpotential of the activated SS7.5 sample is 295 mV at 10 mA cm^{-2}. This overpotential was obtained in a stationary 1 M KOH electrolyte with a scan rate of 5 mV min^{-1} (0.08333 mV s^{-1}) at room temperature. Schäfer et al. [34] reported an overpotential of 212 mV on activated stainless steel at 12 mA cm^{-2} current density in 1 M KOH with a scan rate of 20 mV s^{-1} and stirring (180 r min^{-1}). Todoroki and Wadayama [38] obtained an overpotential of 254 mV in 1 M KOH on activated stainless steel using a rotating disk electrode (1600 rpm) and a scan rate of 5 mV s^{-1} at 20°C. Activated 316 SS sample (SS7.5) linear polarization experiments were assessed by chronopotentiometry (CP) experiments at 10 mA cm^{-2} in 1.0 M KOH for two 24 hours interval followed by LSV. The data showed only minor changes in the performance (see Figure S5).

The estimated double layer capacitances were extracted from cyclic voltammograms (see Figure S6). They were quite similar and found to be 12.1, 12.7, 11.0, 9.7, 9.5, 10.9 and 12.7 µF for SS12.5, SS10, SS7.5, SS5.5, SS3, SS1 and untreated SS316 samples, respectively, in 1.0 M KOH.

A comparison of double layer capacitance values, which is an indirect measure of the electrochemical surface area (ECSA), indicates that the activity cannot be explained by an increase in surface area alone. From the double layer capacitance values it seems apparent that certain surface compositions are more active towards OER than others, which are formed during the electro-oxidation of SS316 in high KOH concentration electrolytes.

3.2. Surface characterization

3.2.1. Surface morphology

Fig. 3 shows high magnification SEM images of the sample surfaces; untreated SS316 (a) SS1 (b), SS5.5 (c) and SS7.5 (d). At this magnification, small, elongated deposits are clearly observed on all activated

samples, in contrast to the apparently smooth untreated SS316 sample. The deposits indicate a roughening of the surface either from dissolution or dissolution and redeposition [31], which would be expected to lead to an increased surface area. However, the double layer capacitance measurements do not indicate a significant change in ECSA after activation. This may be due to i) poor contact between the nanoscale deposits and the substrate, ii) a similar surface roughening of the substrate/untreated sample which is not observed at this magnification, or iii) a significant difference in specific capacitance. Furthermore, it is difficult to assess the electrochemical surface area from SEM images alone [51].

3.2.2. Surface composition

XPS was employed to shed some light on the composition of the oxide surfaces. Table 2 shows the metallic composition of the samples' surfaces, which are composed of Ni, Fe and Cr. These data were obtained using Ni 2*p*, Fe 3*p* and Cr 2*p* from the survey spectra (see Figure S7).

The polished and untreated SS316 sample as well as the mildly etched sample were found to contain only Fe and Cr in the surface, which is in good agreement with the findings of Maurice *et al.* [41] and Olsson *et al.* [46]. Olsson *et al.* explained this phenomenon by arguing that Fe and Cr oxidize more easily than Ni at the metal/oxide interface. Furthermore, it is well-known that iron diffuses more rapidly than chromium within the metal oxide layer [52–55] and this difference in diffusion rate can therefore be used to explain the relatively large fraction of Cr compared to Fe in the surface of the etched sample in comparison to the untreated sample. The etching procedure employed is expected to only remove the outermost layer of the SS surface, which was enriched with Fe due to its faster diffusion. Activating SS316 at +1.70 V in various KOH concentrations changed the surface composition significantly, increasing the Ni content and decreasing the Fe and Cr contents. The compositional change increased further with increasing KOH concentration up to 7.5 M KOH. While the Cr content approaches 0 at 7.5 M KOH and higher, the Fe and Ni contents reached constant values of about 27% and 73%, respectively.

Fig. 4 shows the resulting GD-OES depth profiles for the polished, untreated SS316 and SS7.5 samples. Only Fe and Cr are present at low sputtering times for the untreated sample, with the Ni profile commencing after some delay. This again is an indication that only Fe and Cr are present in the outermost surface, in accordance with the XPS data (Table 2) and cyclic voltammetry (Fig. 1). On the countrary, the Ni intensity was significant at low sputtering times on SS7.5 (after activation), rising simultaenously with the oxygen profile and reached half maximum intensity well before Cr and Fe. The oxide/substrate interface can be represented by the black vertical line, as described by Shimizu *et al.*, taken from the rising edge of the Fe profile, where the signal has intensity equal to half of the maximum intensity of the steady state region [54]. This shows that the surface oxide of untreated SS316 is
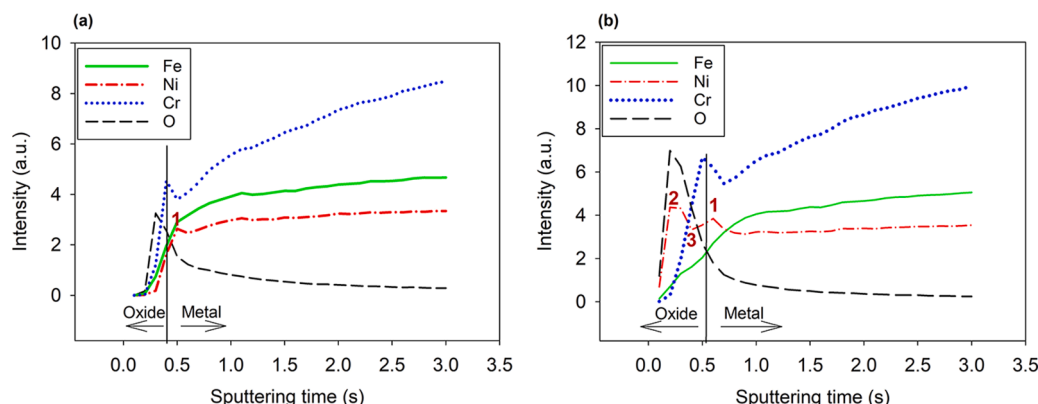

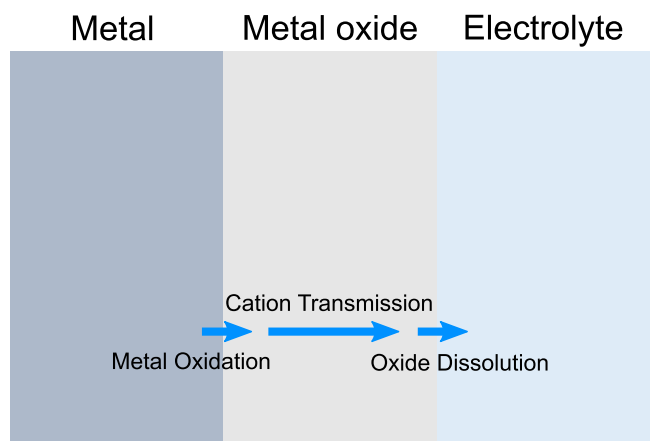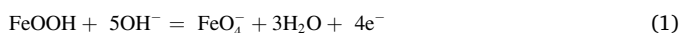**Fig. 4.** GD-OES of the (a) untreated SS316 and (b) SS7.5.

Fig. 5. Schematic representation of three main phenomena on the oxide used in the PDM.

comprised of Cr and Fe when exposed to air and dominated by Ni after activation in 7.5 M KOH. After activation, both the Fe and Cr signals are small at the surface and increase towards the metal substrate. In fact, a maximum is observed for chromium at the inner part of the oxide.

The small Ni peaks underneath the oxide/substrate interface for both samples (red peaks 1 in Fig. 4) suggest that Ni was enriched at top of the metal substrate. Interestingly, the nickel profile for the SS7.5 sample climbs to a maximum at the outer part of the oxide region (indicated as peak 2 in Fig. 4b) before declining and reaching a minimum towards the inner part of the oxide (indicated as 3 in Fig. 4b).

An increase in nickel content at the oxide surface and the depth profile after activation can be justified in terms of the point defect model (PDM) proposed by Macdonald [56]. The PDM considers three main phenomena on the oxide (Fig. 5) (i) metal oxidation at the metal/oxide interface, (ii) transmission of defects (oxygen and cation vacancies as well as interstitials) within the oxide and (iii) dissolution of the oxide film at the oxide/electrolyte interface. The resulting profile is a balance between these three phenomena.

XPS and GD-OES show that applying a high anodic potential at high pH values (CV or activation procedure) leads to an increasing nickel content in the surface oxide. According to the Pourbaix (E-pH) diagrams of Fe-Ni-Cr alloy (see Figure S1), Ni form stable oxides/hydroxides at high pH and potential, while Cr and Fe form soluble complexes (reactions 1 and 2). Therefore, it is expected that any Fe and Cr oxide that make it to the metal oxide/electrolyte interface will oxidize further and dissolve into the electrolyte, while Ni forms a stable oxide under the activation condition. This will result in enrichment of Ni at the outer part of the oxide.

$$FeOOH + 5OH^- = FeO_4^- + 3H_2O + 4e^- \qquad (1)$$

$$CrOOH + 5OH^- = CrO_4^{2-} + 3H_2O + 3e^- \qquad (2)$$

Both Ni and Fe diffuse more rapidly than chromium within the metal oxide layer [52–55], which result in lower Ni and Fe contents, and Cr accumulation in the inner part of the oxide. Olsson and Landot states that Ni is less readily oxidized than Fe and Cr, which will result in Ni being accumulated in its metallic state on top of the metal substrate, i.e. closest to the oxide/metal interface [46].

The PDM model can further be used to explain why the Ni content in the oxide increases with increasing KOH concentration during activation, hence increasing pH. An increase in pH during activation is expected to increase the (i) metal oxidation rates at the metal/oxide interface according to rate expressions outlined by Macdonald [56]. However, the relative oxidation rate of the elements remains the same when assuming the same transfer coefficient. The oxide thickness and the voltage drop across the oxide changes with pH. However, the PDM assumes that the electric field strength remains constant, leading to (ii) transmission rates of defects within the oxide being independent of the oxide thickness and/or voltage drop, and therefore the relative transmission rate of Ni, Fe and Cr cations remains the same and independent of pH. (iii) Dissolution rates of the unstable oxides/hydroxides (Cr and Fe) at the oxide/electrolyte interface increase as the pH rises. However, the Ni oxide/hydroxide stay stable within the pH range and the high potential used in this work. The continuous supply of cations to the metal/oxide interface and the relative stability of Ni oxide/hydroxide in comparison to Fe and Cr at the oxide/electrolyte interface result in an increased amount of Ni at the outer part of the oxide by increasing the pH of the electrolyte. The Fe content reached a constant value of about 27% at 7.5 M KOH and higher, implying that this amount of Fe is stabilized in the presence of nickel, likely being incorporated into the Ni (oxy)hydroxide structure limiting its further dissolution at the given conditions.

The OER overpotential was observed to decrease with increasing Ni content (see Figure S8). The minimum OER overpotential was achieved with about 73% Ni and 27% Fe, similar to the composition for the best performing catalyst obtained previously by Qiu *et al.* [30]. An increase in the Ni content in the vicinity of Fe could be the reason for the higher OER catalytic activities observed for the activated samples. Ni in conjunction with Fe is known to yield improved catalytic activity towards the OER [25].

3.2.3. Surface species

Fig. 6 shows the high-resolution XPS O 1*s*, Fe 3*p* and Ni 2*p*$_{3/2}$ core level spectra measured on the SS7.5 sample. Atomic composition of the layer on SS7.5 was found to be as follows: 5.74% Fe, 15.26% Ni and 79% O.

The Ni 2*p*$_{3/2}$ and Fe 3*p* peak positions at 855.7 eV and 56 eV, respectively, suggest that Ni(II), Ni(III), Fe(II) and Fe (III) are likely to be present in the formed oxide [31,57,58]. A number of oxide phases are possible at the given conditions, such as $Ni(OH)_2$, NiOOH, $NiFe_2O_4$ and
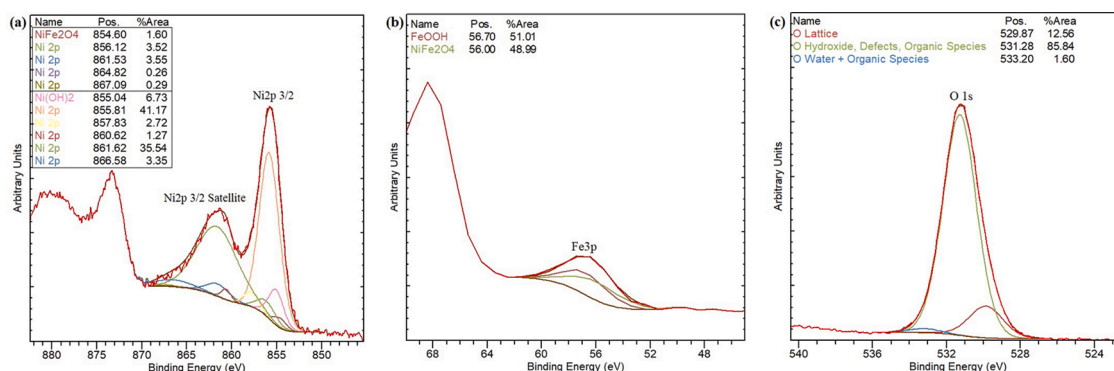

Fig. 6. XPS characterization of SS7.5 sample (a) Ni 2*p*$_{3/2}$, (b) Fe 3*p* and (c) O 1*s*.
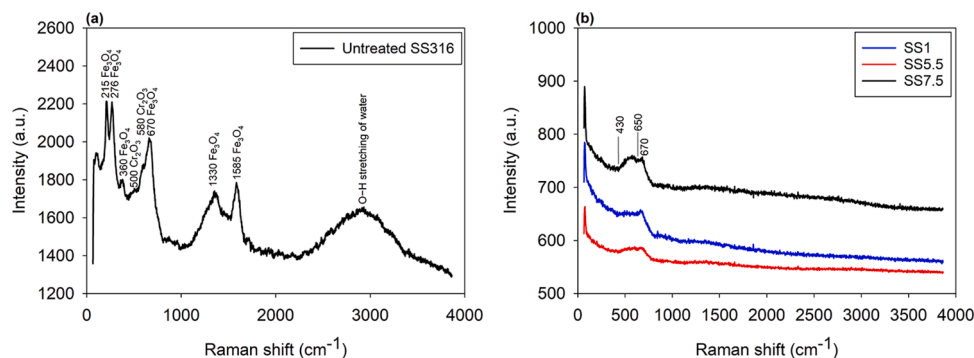
Fig. 7. Raman spectroscopy of the (a) untreated SS316 and (b) treated samples.

Table 3
Surface compositions from XPS of the Ni-Fe alloy and SS3 samples

Sample	Fe ($\pm$4%)	Ni ($\pm$4%)	Cr ($\pm$0.5%)
As-received Ni-Fe	82	18	-
Activated Ni-Fe	46	54	-
SS3	47.1	49.6	3.3

FeOOH [59]. A satisfying fit for the Ni 2p deconvolution in Fig. 6a could not be obtained using only NiOOH or Ni(OH)$_2$ phases alone, nor a combination of the two. Adding NiFe$_2$O$_4$ was necessary to obtain a satisfactorily fit to the Ni 2p, implying that the overall amount of Ni in NiFe$_2$O$_4$ is below 18.8% of the total Ni. Simultaneous fitting of the Ni 2p, Fe 3p and O 1s provided the best fit with 9-16% of Ni in the form of NiFe$_2$O$_4$. Furthermore, the best fit suggested that the oxide is composed of FeOOH, NiFe$_2$O$_4$, Ni(OH)$_2$ and/or NiOOH. Fig. 6a shows the deconvoluted Ni 2p$_{3/2}$ peak fitted with 90.8% Ni(OH)$_2$ and 9.2% NiFe$_2$O$_4$. NiFe$_2$O$_4$ has been claimed to have an essential role in enhancing the OER activity of Fe enriched Ni catalysts, such as NiFe$_2$O$_4$-Fe$_2$O$_3$ and NiFe$_2$O$_4$-NiO mixed phases [25], supporting our finding on activated stainless steel.

Fig. 7 shows the Raman spectra of untreated SS316, SS1, SS5.5 and SS7.5. A sharp peak at 670 cm^{-1} and a broad peak extended from 430 to 650 cm^{-1} are observed for all activated samples. The FeOOH may be present in the oxide as the Raman bands of different FeOOH types is at 670 cm^{-1} [60]. NiOOH has Raman shifts at 470 and 545 cm^{-1} and Ni(OH)$_2$ forms a peak or at least a shoulder at 450 cm^{-1} [60,61]. The main Raman band for all Cr oxide and hydroxide is expected to be found at 580 cm^{-1} [60]. Our Raman spectra, comprising of a broad Raman band and no distinctively sharp Raman peaks for wavelengths from 400 to 650 cm^{-1} suggest that the oxide at the steel surface after activation consists of a disordered oxide composed of a combination of Ni, Fe and Cr oxides. This finding is in good agreement with the study of Ferreira *et al.* study [60], who observed formation of a disordered film on SS316 and SS304 surfaces made of mixed oxide/hydroxide. Louie *et al.* [21], used Raman Spectroscopy analysis and observed some degree of disorder of the catalysts that provided higher OER activity. We believe that such a disorder can contribute to the higher OER activity observed in our work at activated SS316 electrodes.

3.2.4. Effect of Cr on OER

A bulk Ni-Fe alloy (50 at.%-50 at.%) free of Cr was used to assess the effect of chromium on the OER performance of activated SS316. The surface composition of the Ni-Fe alloy before and after activation at +1.70 V for 18 hours in 7.5 M KOH shows a strong increase in the nickel content, from 18 to 54%. The resulting surface nickel composition of the Ni-Fe alloy is similar to the surface nickel composition of sample SS3, activated in 3 M KOH. This finding suggests also that the bulk composition of the substrate plays an important role in the final surface composition, which was recently shown by Todoroki *et al.* [39]. XPS of
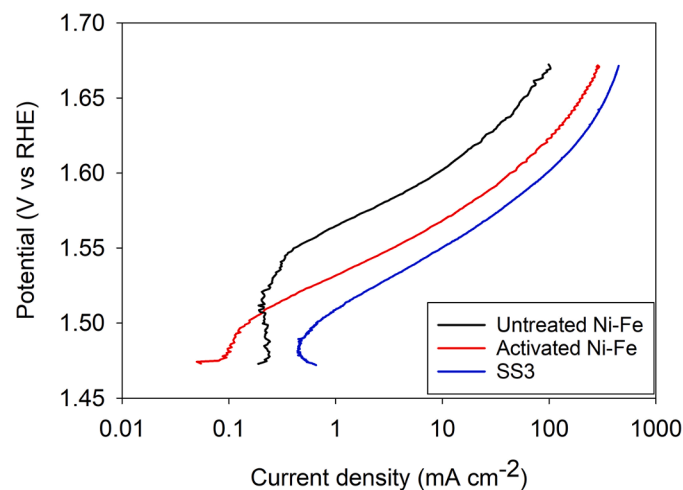

Fig. 8. IR-corrected *E* vs. log(j) curves measured on the Ni-Fe, activated Ni-Fe and SS3 samples in 1.0 M KOH at a scan rate of 5 mV min^{-1}.

both these samples are provided in Table 3. Fig. 8 shows LSVs of the polished as-received Ni-Fe alloy, activated Ni-Fe alloy and SS3 in 1.0 M KOH, averaged over at least two repeats, at a scan rate of 5 mV min^{-1}. The existence of Cr in the oxide appears to have a beneficial effect for the OER performance. Although the Ni-Fe sample has slightly more Ni at the surface compared to SS3, which has some Cr instead, the performance of SS3 is better than the activated Ni-Fe alloy, both being significantly better than the polished as-received Ni-Fe alloy. Minor changes in the double layer capacitances (3.4 µF for polished Ni-Fe and 3.8 µF for activated Ni-Fe) and hence the ECSA after activation, implies that this effect is not due to a change in active surface area alone. Previously, Cr was shown to increase the OER catalytic performance of NiFe$_{2-x}$Cr$_x$O$_4$ (0$\leq$x$\leq$1) in alkaline media [42].

This finding suggests that Cr incorporation into the oxide layer of activated SS316 samples is beneficial for improving OER activity. The exact reasoning for this promoting effect of Cr incorporation is not well understood, but is perhaps related to modification of the electronic structure in favor of improving the OER catalytic activity. Moureaux *et al.* [31] suggested this effect to be a result of a hypo-hyper *d* inter-bonding effect.

3.2.5. Reaction order and Tafel slopes

All SS316 samples, including the untreated sample, have a similar Tafel slope in 1 M KOH (Fig. 2), $b \approx 40$ mV dec^{-1} at low potentials and $b > 120$ mV dec^{-1} at high potentials, suggesting that the OER mechanism on the stainless steel remains unchanged before and after activation and independent of activation electrolyte pH [62]. The LSV of the pure Ni sample is quite different, but the Tafel slope is comparable to SS316 with
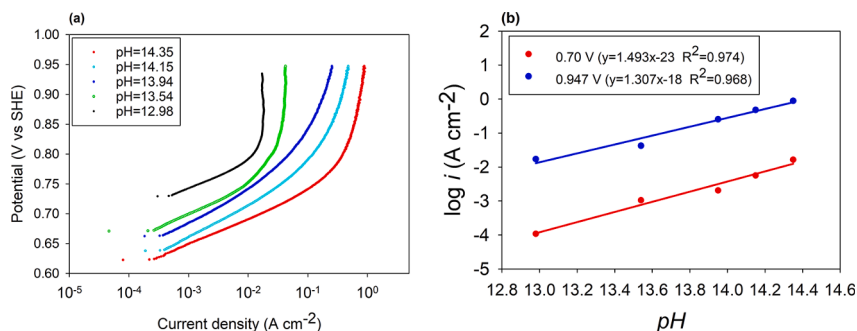
Fig. 9. (a) Polarisation curves E vs. $\log(j)$ measured on the SS7.5 samples at different pHs and at a scan rate of 5 mV s^{-1}. (b) $\log(j)$ versus pH at high ($E = +0.947$ V vs. RHE) and low potentials ($E = +0.7$ V vs. RHE).

44 mV dec^{-1}.

Fig. 9(a) shows the polarization curves measured on the SS7.5 sample in electrolytes with different pH values. Fig. 9(b) shows the corresponding log of current density plot versus pH at high ($E = +0.947$ V vs. SHE) and low potentials ($E = +0.70$ V vs. SHE). The current density at $+0.70$ V for the sample in the electrolyte with pH $= 12.98$ was obtained by extrapolation of Tafel region.

The reaction orders ($m_{x,V}$) versus a pH-independent reference electrode (SHE) for SS7.5 sample were found to be 1.492 and 1.307 for low and high potential values, respectively.

The different Tafel behavior at low and high potentials could be due to either surface coverage or change in the rate-determining step (rds) [63]. The observed fractional reaction orders could be due to the competition between several reaction pathways or side reactions at the electrode surface [64,65]. Fractional reaction orders have also been suggested to be related to other effects, such as adsorption of charged species on the electrode surface and variations in the electrical potential gradient or blocking effects [64–66]. It is well-known that the potential distribution in the double layer affects the rate of the reaction since this distribution influences the rate constant and concentration of the reacting species at the site where electron transfer takes place [64].

It is therefore not straightforward to assign a reaction mechanism, however, the Tafel slope of 40 mV dec^{-1} and the reaction order of 1.492 at low potentials match well with mechanisms where the rds involves transfer of one electron (formation of a higher valance state of the metal ion) in conjunction with the transfer of one additional electron in a preceding step, before the rds. Moreover, a Tafel slope of 40 mV dec^{-1} and a reaction order of 1.492 match the values for an aged Fe oxide layer reported by Lyons and Doyle [67] (b$\approx$ 40 mV dec^{-1} and $m_{OH^-} = 1.5$). A Tafel slope of 42 mV dec^{-1} and a reaction order of 1 have previously been reported for pure Ni [20,21], suggesting a different reaction mechanism than on SS316 surfaces.

4. Conclusions

Stainless steel 316 was activated through electro-oxidation at a constant potential of $+1.70$ V vs. RHE. It was found that the pre-treatment electrolyte concentration influences the surface composition and hence the catalytic activity. The Ni content in the activated samples increased from 41% when activated in 1 M KOH up to 73% when activated in 7.5 M KOH or higher. The increase in nickel content with KOH concentration can be understood in terms of the point defect model, with the dissolution rate of metal oxides being the primary reason for the increase in Ni content.

Samples activated in 7.5 M KOH and higher exhibited the best activity towards oxygen evolution, with a potential of $+1.525$ V vs. RHE at 10 mA cm^{-2}. The oxide surface on samples activated in 7.5 M KOH is composed of Ni and Fe oxides only, suggested to be FeOOH, NiFe$_2$O$_4$, Ni (OH)$_2$ and/or NiOOH. The presence of Cr in the surface or sub-surface oxide is found to be beneficial for the oxygen evolution reaction in 1

M KOH. A Tafel slope of about 40 mV dec^{-1} was observed for all stainless steel samples in 1 M KOH, suggesting the same mechanism for all surface compositions. A reaction order of 1.492 and 1.307 were found at the samples activated in 7.5 M at low and high potentials, respectively.

CRediT authorship contribution statement

Hamid Reza Zamanizadeh: Conceptualization, Data curation, Formal analysis, Investigation, Methodology, Visualization, Writing – original draft, Writing – review & editing. **Svein Sunde:** Supervision, Conceptualization, Writing – review & editing, Validation. **Bruno G. Pollet:** Supervision, Conceptualization, Writing – review & editing, Validation. **Frode Seland:** Supervision, Project administration, Conceptualization, Validation, Resources, Writing – review & editing, Funding acquisition.

Declaration of Competing Interest

The authors declare that they have no known competing financial interests or personal relationships that could have appeared to influence the work reported in this paper.

Supplementary materials

Supplementary material associated with this article can be found, in the online version, at doi:10.1016/j.electacta.2022.140561.

References

[1] S. Trasatti, Electrocatalysis in the anodic evolution of oxygen and chlorine, Electrochimica Acta 29 (11) (1984) 1503–1512.

[2] A. Grimaud, O. Diaz-Morales, B. Han, W.T. Hong, Y.-L. Lee, L. Giordano, K. A. Stoerzinger, M.T. Koper, Y. Shao-Horn, Activating lattice oxygen redox reactions in metal oxides to catalyse oxygen evolution, Nature chemistry 9 (5) (2017) 457–465.

[3] I.C. Man, H.Y. Su, F. Calle-Vallejo, H.A. Hansen, J.I. Martínez, N.G. Inoglu, J. Kitchin, T.F. Jaramillo, J.K. Nørskov, J. Rossmeisl, Universality in oxygen evolution electrocatalysis on oxide surfaces, ChemCatChem 3 (7) (2011) 1159–1165.

[4] L. Han, S. Dong, E. Wang, Transition-metal (Co, Ni, and Fe)-based electrocatalysts for the water oxidation reaction, Advanced materials 28 (42) (2016) 9266–9291.

[5] R. Singh, J. Singh, A. Singh, Electrocatalytic properties of new spinel-type MMoO4 (M= Fe, Co and Ni) electrodes for oxygen evolution in alkaline solutions, international journal of hydrogen energy 33 (16) (2008) 4260–4264.

[6] F. Song, L. Bai, A. Moysiadou, S. Lee, C. Hu, L. Liardet, X. Hu, Transition metal oxides as electrocatalysts for the oxygen evolution reaction in alkaline solutions: an application-inspired renaissance, Journal of the American Chemical Society 140 (25) (2018) 7748–7759.

[7] E. Fabbri, A. Habereder, K. Waltar, R. Kötz, T.J. Schmidt, Developments and perspectives of oxide-based catalysts for the oxygen evolution reaction, Catalysis Science & Technology 4 (11) (2014) 3800–3821.

[8] I. Katsounaros, S. Cherevko, A.R. Zeradjanin, K.J. Mayrhofer, Oxygen electrochemistry as a cornerstone for sustainable energy conversion, Angewandte Chemie International Edition 53 (1) (2014) 102–121.

[9] A.D. Doyle, M. Bajdich, A. Vojvodic, Theoretical insights to bulk activity towards oxygen evolution in oxyhydroxides, Catalysis Letters 147 (6) (2017) 1533–1539.

[10] J.O.'M. Bockris, T. Otagawa, The electrocatalysis of oxygen evolution on perovskites, Journal of The Electrochemical Society 131 (2) (1984) 290.

[11] X. Li, F.C. Walsh, D. Pletcher, Nickel based electrocatalysts for oxygen evolution in high current density, alkaline water electrolysers, Physical Chemistry Chemical Physics 13 (3) (2011) 1162–1167.

[12] M.D. Merrill, R.C. Dougherty, Metal oxide catalysts for the evolution of O_2 from H_2O, The Journal of Physical Chemistry C 112 (10) (2008) 3655–3666.

[13] L. Trotochaud, J.K. Ranney, K.N. Williams, S.W. Boettcher, Solution-cast metal oxide thin film electrocatalysts for oxygen evolution, Journal of the American Chemical Society 134 (41) (2012) 17253–17261.

[14] D.A. Corrigan, R.M. Bendert, Effect of coprecipitated metal ions on the electrochemistry of nickel hydroxide thin films: cyclic voltammetry in 1M KOH, Journal of The Electrochemical Society 136 (3) (1989) 723–728.

[15] R.L. Tichenor, Nickel Oxides-Relation Between Electrochemical and Foreign Ion Content, Industrial & Engineering Chemistry 44 (5) (1952) 973–977.

[16] M.S. Burke, L.J. Enman, A.S. Batchellor, S. Zou, S.W. Boettcher, Oxygen evolution reaction electrocatalysis on transition metal oxides and (oxy) hydroxides: activity trends and design principles, Chemistry of Materials 27 (22) (2015) 7549–7558.

[17] S. Klaus, Y. Cai, M.W. Louie, L. Trotochaud, A.T. Bell, Effects of Fe electrolyte impurities on Ni (OH) 2/NiOOH structure and oxygen evolution activity, The Journal of Physical Chemistry C 119 (13) (2015) 7243–7254.

[18] D.A. Corrigan, The catalysis of the oxygen evolution reaction by iron impurities in thin film nickel oxide electrodes, Journal of The Electrochemical Society 134 (2) (1987) 377–384.

[19] G. Młynarek, M. Paszkiewicz, A. Radniecka, The effect of ferric ions on the behaviour of a nickelous hydroxide electrode, Journal of applied electrochemistry 14 (2) (1984) 145–149.

[20] M.E. Lyons, M.P. Brandon, The oxygen evolution reaction on passive oxide covered transition metal electrodes in aqueous alkaline solution. Part 1-Nickel, Int. J. Electrochem. Sci 3 (12) (2008) 1386–1424.

[21] M.W. Louie, A.T. Bell, An investigation of thin-film Ni–Fe oxide catalysts for the electrochemical evolution of oxygen, Journal of the American Chemical Society 135 (33) (2013) 12329–12337.

[22] L. Trotochaud, S.L. Young, J.K. Ranney, S.W. Boettcher, Nickel–iron oxyhydroxide oxygen-evolution electrocatalysts: the role of intentional and incidental iron incorporation, Journal of the American Chemical Society 136 (18) (2014) 6744–6753.

[23] M. Gong, H. Dai, A mini review of NiFe-based materials as highly active oxygen evolution reaction electrocatalysts, Nano Research 8 (1) (2015) 23–39.

[24] Z. Lu, W. Xu, W. Zhu, Q. Yang, X. Lei, J. Liu, Y. Li, X. Sun, X. Duan, Three-dimensional NiFe layered double hydroxide film for high-efficiency oxygen evolution reaction, Chemical communications 50 (49) (2014) 6479–6482.

[25] J. Landon, E. Demeter, N. Inoglu, C. Keturakis, I.E. Wachs, R. Vasic, A.I. Frenkel, J. R. Kitchin, Spectroscopic characterization of mixed Fe–Ni oxide electrocatalysts for the oxygen evolution reaction in alkaline electrolytes, Acs Catalysis 2 (8) (2012) 1793–1801.

[26] D. Friebel, M.W. Louie, M. Bajdich, K.E. Sanwald, Y. Cai, A.M. Wise, M.-J. Cheng, D. Sokaras, T.-C. Weng, R. Alonso-Mori, Identification of highly active Fe sites in (Ni, Fe) OOH for electrocatalytic water splitting, Journal of the American Chemical Society 137 (3) (2015) 1305–1313.

[27] H.S. Ahn, A.J. Bard, Surface Interrogation Scanning Electrochemical Microscopy of Ni1−x Fe x OOH (0< x< 0.27) Oxygen Evolving Catalyst: Kinetics of the "Fast" Iron Sites, Journal of the American Chemical Society 138 (1) (2016) 313–318.

[28] R. Singh, J. Pandey, K. Anitha, Preparation of electrodeposited thin films of nickel-iron alloys on mild steel for alkaline water electrolysis. Part I: Studies on oxygen evolution, International journal of hydrogen energy 18 (6) (1993) 467–473.

[29] M. Görlin, P. Chernev, J. Ferreira de Araújo, T. Reier, S.r. Dresp, B. Paul, R. Krähnert, H. Dau, P. Strasser, Oxygen evolution reaction dynamics, faradaic charge efficiency, and the active metal redox states of Ni–Fe oxide water splitting electrocatalysts, Journal of the American Chemical Society 138 (17) (2016) 5603–5614.

[30] Y. Qiu, L. Xin, W. Li, Electrocatalytic oxygen evolution over supported small amorphous Ni–Fe nanoparticles in alkaline electrolyte, Langmuir 30 (26) (2014) 7893–7901.

[31] F. Moureaux, P. Stevens, G. Toussaint, M. Chatenet, Development of an oxygen-evolution electrode from 316L stainless steel: Application to the oxygen evolution reaction in aqueous lithium–air batteries, Journal of power sources 229 (2013) 123–132.

[32] H. Schäfer, S.M. Beladi-Mousavi, L. Walder, J. Wollschläger, O. Kuschel, S. Ichilmann, S. Sadaf, M. Steinhart, K. Küpper, L. Schneider, Surface oxidation of stainless steel: oxygen evolution electrocatalysts with high catalytic activity, ACS Catalysis 5 (4) (2015) 2671–2680.

[33] H. Schäfer, D.M. Chevrier, P. Zhang, J. Stangl, K. Müller-Buschbaum, J.D. Hardege, K. Kuepper, J. Wollschläger, U. Krupp, S. Dühnen, Electro-Oxidation of Ni42 Steel:

[34] A Highly Active Bifunctional Electrocatalyst, Advanced Functional Materials 26 (35) (2016) 6402–6417.

[34] H. Schäfer, S. Sadaf, L. Walder, K. Kuepper, S. Dinklage, J. Wollschläger, L. Schneider, M. Steinhart, J. Hardege, D. Daum, Stainless steel made to rust: a robust water-splitting catalyst with benchmark characteristics, Energy & Environmental Science 8 (9) (2015) 2685–2697.

[35] S. Anantharaj, M. Venkatesh, A.S. Salunke, T.V. Simha, V. Prabu, S. Kundu, High-performance oxygen evolution anode from stainless steel via controlled surface oxidation and Cr removal, ACS Sustainable Chemistry & Engineering 5 (11) (2017) 10072–10083.

[36] H. Zhong, J. Wang, F. Meng, X. Zhang, In situ activating ubiquitous rust towards low-cost, efficient, free-standing, and recoverable oxygen evolution electrodes, Angewandte Chemie International Edition 55 (34) (2016) 9937–9941.

[37] H. Schäfer, M. Chatenet, Steel: the resurrection of a forgotten water-splitting catalyst, ACS Energy Letters 3 (3) (2018) 574–591.

[38] N. Todoroki, T. Wadayama, Heterolayered Ni–Fe hydroxide/oxide nanostructures generated on a stainless-steel substrate for efficient alkaline water splitting, ACS Applied Materials & Interfaces 11 (47) (2019) 44161–44169.

[39] N. Todoroki, A. Shinomiya, T. Wadayama, Nanostructures and Oxygen Evolution Overpotentials of Surface Catalyst Layers Synthesized on Various Austenitic Stainless Steel Electrodes, Electrocatalysis (2022) 1–10.

[40] N. Todoroki, T. Wadayama, Electrochemical stability of stainless-steel-made anode for alkaline water electrolysis: Surface catalyst nanostructures and oxygen evolution overpotentials under applying potential cycle loading, Electrochemistry Communications 122 (2021), 106902.

[41] V. Maurice, W. Yang, P. Marcus, X-Ray photoelectron spectroscopy and scanning tunneling microscopy study of passive films formed on (100) Fe-18Cr-13Ni single-crystal surfaces, Journal of the Electrochemical Society 145 (3) (1998) 909.

[42] R. Singh, J. Singh, B. Lal, M. Thomas, S. Bera, New NiFe2− xCrxO4 spinel films for O_2 evolution in alkaline solutions, Electrochimica acta 51 (25) (2006) 5515–5523.

[43] F. Moureaux, P. Stevens, G. Toussaint, M. Chatenet, Timely-activated 316L stainless steel: A low cost, durable and active electrode for oxygen evolution reaction in concentrated alkaline environments, Applied Catalysis B: Environmental 258 (2019), 117963.

[44] I. Hamidah, A. Solehudin, A. Setiawan, A. Hamdani, M.A.S. Hidayat, F. Adityawarman, F. Khoirunnisa, A.B.D. Nandiyanto, Corrosion study of AISI 304 on KOH, NaOH, and NaCl solution as an electrode on electrolysis process, Journal of Engineering Science and Technology 13 (5) (2018) 1345–1351.

[45] L. Freire, M.A. Catarino, M. Godinho, M. Ferreira, M. Ferreira, A. Simões, M. Montemor, Electrochemical and analytical investigation of passive films formed on stainless steels in alkaline media, Cement and Concrete Composites 34 (9) (2012) 1075–1081.

[46] C.-O. Olsson, D. Landolt, Passive films on stainless steels—chemistry, structure and growth, Electrochimica acta 48 (9) (2003) 1093–1104.

[47] M. Kölbach, S. Fiechter, R. van de Krol, P. Bogdanoff, Evaluation of electrodeposited α-Mn2O3 as a catalyst for the oxygen evolution reaction, Catalysis Today 290 (2017) 2–9.

[48] C. Abreu, M. Cristóbal, R. Losada, X. Nóvoa, G. Pena, M. Pérez, The effect of Ni in the electrochemical properties of oxide layers grown on stainless steels, Electrochimica Acta 51 (15) (2006) 2991–3000.

[49] M. Alsabet, M. Grdeń, G. Jerkiewicz, Electrochemical growth of surface oxides on nickel. Part 3: Formation of β-NiOOH in relation to the polarization potential, polarization time, and temperature, Electrocatalysis 6 (1) (2015) 60–71.

[50] M.S. Burke, M.G. Kast, L. Trotochaud, A.M. Smith, S.W. Boettcher, Cobalt–iron (oxy) hydroxide oxygen evolution electrocatalysts: the role of structure and composition on activity, stability, and mechanism, Journal of the American Chemical Society 137 (10) (2015) 3638–3648.

[51] U.P. Do, F. Seland, E.A. Johannessen, The real area of nanoporous catalytic surfaces of gold and palladium in aqueous solutions, Journal of The Electrochemical Society 165 (3) (2018) H219.

[52] J. Huang, X. Wu, E.-H. Han, Electrochemical properties and growth mechanism of passive films on Alloy 690 in high-temperature alkaline environments, Corrosion Science 52 (10) (2010) 3444–3452.

[53] W. Li, Z. Mi, S. Qin, L. Gao, J. He, L. Guo, L. Qiao, CS-AFM study on Pb-induced degradation of passive film on nickel-based alloy in high temperature and high pressure water, Corrosion Science 144 (2018) 249–257.

[54] K. Shimizu, H. Habazaki, P. Skeldon, G. Thompson, G. Wood, GDOES depth profiling analysis of the air-formed oxide film on a sputter-deposited Type 304 stainless steel, Surface and Interface Analysis: An International Journal devoted to the development and application of techniques for the analysis of surfaces, interfaces and thin films 29 (11) (2000) 743–746.

[55] K. Shimizu, H. Habazaki, P. Skeldon, G. Thompson, Impact of RF-GD-OES in practical surface analysis, Spectrochimica Acta Part B: Atomic Spectroscopy 58 (9) (2003) 1573–1583.

[56] D.D. Macdonald, The history of the point defect model for the passive state: a brief review of film growth aspects, Electrochimica Acta 56 (4) (2011) 1761–1772.

[57] N. McIntyre, D. Zetaruk, X-ray photoelectron spectroscopic studies of iron oxides, Analytical Chemistry 49 (11) (1977) 1521–1529.

[58] A. Grosvenor, B. Kobe, M. Biesinger, N. McIntyre, Investigation of multiplet splitting of Fe 2p XPS spectra and bonding in iron compounds, Surface and Interface Analysis: An International Journal devoted to the development and application of techniques for the analysis of surfaces, interfaces and thin films 36 (12) (2004) 1564-1574.

[59] T. Naoto, Atlas of Eh-pH diagrams. Intercomparison of thermodynamic databases, Geological Survey of Japan Open File Report 419 (2005) 154–155.

[60] M. Ferreira, T.M. e Silva, A. Catarino, M. Pankuch, C. Melendres, Electrochemical and laser Raman spectroscopy studies of stainless steel in 0.15 M NaCl solution, Journal of the Electrochemical Society 139 (11) (1992) 3146–3151.

[61] S. Cordoba-Torresi, A. Hugot-Le Goff, S. Joiret, Electrochromic behavior of nickel oxide Electrodes II. Identification of the bleached state by Raman spectroscopy and nuclear reactions, Journal of the Electrochemical Society 138 (6) (1991) 1554–1559.

[62] M.E. Lyons, M.P. Brandon, A comparative study of the oxygen evolution reaction on oxidised nickel, cobalt and iron electrodes in base, Journal of Electroanalytical Chemistry 641 (1-2) (2010) 119–130.

[63] R.L. Doyle, M.E. Lyons, The oxygen evolution reaction: mechanistic concepts and catalyst design. Photoelectrochemical solar fuel production, Springer, 2016, pp. 41–104.

[64] A.H. Reksten, H. Thuv, F. Seland, S. Sunde, The oxygen evolution reaction mechanism at IrxRu1− xO2 powders produced by hydrolysis synthesis, Journal of Electroanalytical Chemistry 819 (2018) 547–561.

[65] L. Giordano, B. Han, M. Risch, W.T. Hong, R.R. Rao, K.A. Stoerzinger, Y. Shao-Horn, pH dependence of OER activity of oxides: current and future perspectives, Catalysis Today 262 (2016) 2–10.

[66] C. Angelinetta, M. Falciola, S. Trasatti, Heterogenous acid-base equilibria and reaction order of oxygen evolution on oxide electrodes, Journal of electroanalytical chemistry and interfacial electrochemistry 205 (1-2) (1986) 347–353.

[67] M.E. Lyons, R.L. Doyle, Oxygen evolution at oxidised iron electrodes: a tale of two slopes, Int. J. Electrochem. Sci 7 (10) (2012) 9488–9501.